applied sciences

MDPI

Article

Compensation of Limited Bandwidth and Nonlinearity for Coherent Transponder

Qiang Wang, Yang Yue * and Jon Anderson

Juniper Networks, 1133 Innovation Way, Sunnyvale, CA 94089, USA; qiwang.thresh@gmail.com (Q.W.); jonanderson@juniper.net (J.A.)

* Correspondence: yyue@juniper.net; Tel.: +1-408-745-2000

Received: 27 March 2019; Accepted: 23 April 2019; Published: 28 April 2019

Abstract: Coherent optical transponders are widely deployed in today's long haul and metro optical networks using dense wavelength division multiplexing. To increase the data carrying capacity, the coherent transponder utilizes the high order modulation format and operates at a high baud rate. The limited bandwidth and the nonlinearity are two critical impairments for the coherent in-phase quadrature transmitter. These impairments can be mitigated by digital filters. However, to accurately determine the coefficients of these filters is difficult because the impairment from the limited bandwidth and the impairment from nonlinearity are coupled together. In this paper, we present a novel method to solve this problem. During the initial power-up, we apply a sinusoidal stimulus to the coherent IQ transmitter. We then scan the frequency and amplitude of the stimulus and monitor the output power. By curve-fitting with an accurate mathematical model, we determine the limited bandwidth, the nonlinearity, the power imbalance, and the bias point of the transponder simultaneously. Optimized coefficients of the digital filters are determined accordingly. Furthermore, we utilize a coherent IQ transponder and demonstrate that the limited bandwidth is improved by the finite impulse response filter, while nonlinearity is mitigated by the memoryless Volterra filter.

Keywords: coherent communication; optical communication; pluggable module

1. Introduction

Today's telecommunications infrastructure relies on optical fiber communications systems where the coherent in-phase quadrature (IQ) optical transceiver is an essential component. To deliver a large amount of information over a long distance, the high-order quadrature amplitude modulation (QAM) running at a high baud-rate has been adopted in the long-haul transmission system [1,2]. The information is carried on two orthogonal domains. One domain is the in-phase (I) and quadrature (Q), and the other domain is the two orthogonal polarizations, which are X and Y. Thus, four tributary channels are formed, namely XI, XQ, YI, and YQ. Within each tributary, there are impairments due to the limited bandwidth and nonlinearity. Among these tributaries, there are degrading effects due to the time skew and power imbalance. In this work, we mainly focus on the impairments within each tributary.

The limited bandwidth ultimately determines the highest achievable baud rate of the coherent IQ transponder. It is critical to compensate for the limited bandwidth, particularly for the high baud rate coherent IQ transponder. For example, the state-of-art system runs at the all-electronically multiplexed symbol rate of 180 GBd (giga baud) [3]. The nonlinearity causes uneven distribution of the constellation points in the complex plane and eventually limits the signal-to-noise ratio (SNR). Thus, it is equally important to mitigate the nonlinearity for the coherent IQ transponder using the high order QAM. As an example, the next generation coherent DWDM system uses the probability shaping constellation (PSC) QAM [4], and the state-of-the-art demonstration utilizes 4096-PSC-QAM [5].

The limited bandwidth is usually mitigated by the finite impulse response (FIR) filter through the pre-emphasis process in the digital domain. For example, a 61 GBd coherent system can still be demonstrated when the overall electrical bandwidth of the coherent IQ transceiver is less than 15 GHz [6]. To set the FIR filter, one needs to measure the system's bandwidth accurately. A traditional method is to apply a stimulus, for example a sinusoidal signal, to the Mach–Zehnder modulator (MZM). By scanning the frequency of the stimulus and measuring the optical power from the output of MZM, one can determine its bandwidth. To limit the influence of the nonlinearity, the sinusoidal signal has a small amplitude. However, the actual analog signal generated by real data is a large signal applied to the MZM to utilize the dynamic range of the coherent IQ transmitter fully. On the other hand, the bandwidth measured with a large signal is influenced by the nonlinearity, making the measurement result inaccurate.

Multiple methods have been demonstrated to mitigate the nonlinearity. In [7], a lightwave component analyzer is used to determine the limited bandwidth by performing a small-signal measurement. The limited bandwidth is compensated by the first-order kernel of the Volterra filter. Next, the constellation diagram is recovered by the coherent receiver through the digital signal processing (DSP). The second-order kernel and the third-order kernel of the Volterra filters are adaptively updated through the indirect learning algorithm. In such a routine, the nonlinearity is mitigated by minimizing the error function. In [8], the indirect learning algorithm is further expanded so that the limited bandwidth, the time skew between the in-phase tributary and the quadrature tributary, and the nonlinearity are simultaneously compensated by the Volterra filter. In [9], the limited bandwidth, the time skew, and the nonlinearity are simultaneously detected by a high-speed photodiode and a sampling oscilloscope. The high-order Volterra filter is used to compensate those impairments. In [10], a look-up table (LUT) mitigates the nonlinearity and pattern-dependent distortion. The 7-symbol LUT is trained by determining the difference between the training symbol and the actual sample value for the signal. The known symbol sequence is identified by a sliding window, and the address of the LUT is formed accordingly.

Although those developed methods can mitigate the nonlinearity, they rely on the high-speed photodiode to perform optical-to-electrical conversion, and the high-speed digital-to-analog converter (DAC) to perform the measurement. The setup is complicated and cannot be easily integrated within the coherent transponder.

In this article, we demonstrate a novel method to compensate for the limited bandwidth and mitigate the nonlinearity. The most significant advantage of the proposed technique is a simple setup using the low-speed photodiode integrated into the coherent transponder. First, we establish an accurate mathematical model describing the output from the MZM, taking into consideration the limited bandwidth and the nonlinearity. Next, during the initial phase of the coherent transponder, we demonstrate the simultaneous measurement of the limited bandwidth, the nonlinearity, the power imbalance, and the bias point. From the measurement result, we determine the coefficients of the FIR filter and the memoryless Volterra filter. Finally, we compensate for the limited bandwidth and mitigate the nonlinearity of the coherent transmitter.

The article is organized as follows: In Section 2, we establish the mathematic model; in Section 3, we show the measurement result and demonstrate the compensation of the limited bandwidth and the nonlinearity; in Section 4, we discuss multiple aspects of the proposed technique; in Section 5, we draw the conclusions.

The presence of bandwidth limitation and nonlinearity is not unique to the coherent optical transponder. In other types of application, such as radio over fiber [11,12] and millimeter wave band communication [13,14], the transmitter also suffers from the penalty due to bandwidth limitation and nonlinearity. Thus, the novel method demonstrated in this paper can be adopted, modified, and applied to different types of communication systems.

2. Principle

Figure 1 shows a typical coherent IQ transmitter which consists of the digital signal processing (DSP) application specific integrated circuit (ASIC) and the analog coherent optics (ACO). The layer of forward error correction (FEC) adds the overhead error correction. Next, an FIR filter in the tap-and-delay structure compensates the limited bandwidth. The FIR filter is $T_s/2$ spaced, where T_s is the symbol period. A high-speed DAC converts the output of the FIR filter from the digital domain to the analog domain. It is also possible to implement a nonlinear equalizer like the Volterra filter to mitigate the nonlinearity. The analog electrical signal goes through the traces on the radio-frequency (RF) print circuit board (PCB), the pluggable interface (if applicable), the linear RF amplifiers and then are finally applied to the MZM.

The DAC, the RF trace on the PCB, the pluggable connector, the RF electrical amplifier, and the MZM contribute to the limited bandwidth. The intrinsic transfer function of MZM in the form of sinusoidal function and the nonlinear amplitude response within the data path contribute to the nonlinearity.

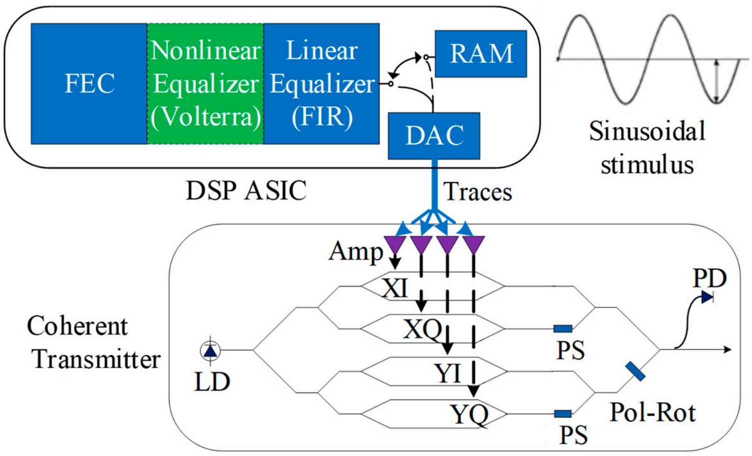

Figure 1. The block diagram of the coherent IQ transmitter and the DSP ASIC. PS: phase shifter, Pol-Rot: polarization rotator. DAC input can be switched between RAM and regular path.

Also, an onboard random-access memory (RAM) can be implemented in the DSP ASIC for testing and diagnosis. During the initial calibration, one can load RAM with the desired data pattern, and set the output of the DAC according to the content in the RAM. After the initial calibration, one can switch back to the regular data path. We utilize this feature to demonstrate our technique. Initially, during the power-up, we load the RAM with a sinusoidal stimulus to one tributary at a time and write 0 to the other tributaries. Thus, the output is from the tributary with the stimulus. Then, we can apply the following equation

$$P_{out} = P_{stdy} \cos^2\left(0.5\pi(V_{swing}/V_\pi + V_{bias}/V_{null})\right), \quad (1)$$

here P_{out} is the output from the IQ transmitter, monitored by a low-speed photodiode (PD). P_{stdy} is the steady-state power of the tributary under stimulus, V_{swing} is the voltage applied to the MZM, V_π is the voltage achieving π phase shift, V_{bias} is the bias voltage applied to MZM, V_{null} is the bias voltage required for the null point (corresponding to $\pi/2$ phase shift), $cos^2()$ is the intrinsic transfer function of the MZM.

V_{DAC} is the maximum output voltage of the DAC, IL_{RF} is the insertion loss of the RF traces, $Gain_{AMP}$ is the gain of the RF amplifier, BW_{MZM} is the bandwidth of the MZM. The parameters above are frequency-dependent and thus contribute to the limited bandwidth. N_{sig} and ω are the amplitude and frequency of the sinusoidal stimulus. Bit_{DAC} is the number of bits of the high-speed DAC, where the first bit is a sign bit. Consequently, V_{swing} can be expressed as the following:

$$\begin{aligned} V_{swing} = N_{sig}\sin(\omega t) * V_{DAC}(\omega) * IL_{RF}(\omega) \\ *Gain_{AMP}(\omega) * BW_{MZM}(\omega)/2^{(Bit_{DAC}-1)} \end{aligned}, \tag{2}$$

Furthermore, we define the normalized signal amplitude x, the bandwidth factor α, the bias factor β, and the MZM phase shift φ_{MZM}. The output from the MZM is expressed as

$$\begin{aligned} & x = N_{sig}/2^{(Bit_{DAC}-1)}, x \in [0,1), \\ & \alpha_\omega = V_{DAC} * IL_{RF} * Gain_{AMP} * BW_{MZM}/V_\pi, \\ & \beta = V_{bias}/V_{null}, \\ & \phi_{mzm} = 0.5\pi\alpha_\omega x \sin(\omega t), \\ & P_{out}(\omega, x) = P_{stdy}\cos^2(\phi_{mzm} + 0.5\pi\beta) \end{aligned}, \tag{3}$$

The nonlinear amplitude response is not included in Equation (3). In [15,16], the nonlinear response is treated as a quadrature term in x. Adding nonlinear response, φ_{mzm} is expressed as

$$\phi_{mzm} = 0.5\pi\alpha_\omega\left(\gamma_\omega x^2 + x\right)\sin(\omega t), \tag{4}$$

here γ is the coefficient for a nonlinear response. The subscript of α and γ indicates that they are dependent on the frequency.

Using the Jacobi–Anger expansion [17], one can show that Equation (4) can be written as the following

$$\begin{aligned} & P_{out}(\omega, x) = 0.5P_{stdy} + 0.5P_{stdy}\cos(\pi\beta)J_0\left(\pi\alpha_\omega\left(\gamma_\omega x^2 + x\right)\right) \\ & +P_{stdy}\cos(\pi\beta)\sum_{m=1}^{\infty} J_{2m}\left(\pi\alpha_\omega\left(\gamma_\omega x^2 + x\right)\right)\cos(2m\omega t) \\ & -P_{stdy}\sin(\pi\beta)\sum_{m=1}^{\infty} J_{2m-1}\left(\pi\alpha_\omega\left(\gamma_\omega x^2 + x\right)\right)\sin((2m-1)\omega t) \end{aligned}, \tag{5}$$

here, $J_m(\ )$ is the first-kind m-th Bessel function. The average output power over the time $P_{avg}(\omega,x)$, detected by a low-speed PD, can be expressed as

$$P_{avg}(\omega, x) = 0.5P_{stdy}\left[1 + \cos(\pi\beta)J_0\left(\pi\alpha_\omega\left(\gamma_\omega x^2 + x\right)\right)\right], \tag{6}$$

We fix ω and scan the amplitude of the sinusoidal stimulus between 0 and 2^(Bit_{ADC}-1). We get a curve of $P_{avg}(\omega,x)$ versus x. The underlying fitting parameter [P_{stdy}, α_ω, β, γ_ω] can be extracted using a curve fitting method like sequential quadratic programming (SQP). The SQP minimizes the relative root-mean-square (RMS) error

$$Err_{rms} = \frac{\sum_{k=1}^{K}\left[P_{avg}^{Meas}(x_k) - P_{avg}^{Fit}(x_k)\right]^2}{K\left[P_{avg}^{Meas}(x_k)\right]^2}, \tag{7}$$

where superscript "*Meas*" and "*Fit*" indicate the measurement results and the fitting results. Here K and k are the total measurements and the index of measurement.

Next, we scan the frequency from a value close to DC (for example, a few GHz) to the value of the baud rate. We record the optical power from each tributary when the amplitude of the sinusoidal stimulus is varied from zero to full swing. We perform the curve fitting according to Equations (6) and (7). Then, we determine the α_ω and γ_ω over the different frequencies. Accordingly, we find the coefficients of the FIR filter and Volterra filter to mitigate the limited bandwidth and the nonlinearity. Furthermore, the power imbalance between tributaries and the bias point of the MZM can be decided by P_{stdy} and β. The DAC's input returns to the regular data path for normal operation after the impairments are calibrated.

3. Experimental Results

3.1. Measured Bandwidth and Nonlinearity

The proposed technique is validated on a pluggable CFP2-ACO module (CFP2 form factor analog coherent optics) and a DSP ASIC [18]. The pluggable module is a class-2 CFP2-ACO with a linear RF amplifier, which can support 200 Gb/s (gigabit per second) traffic using 16-QAM or 300 Gb/s traffic using 64-QAM, at the baud rate of ~30 GBd. The DSP ASIC has the built-in RAM, allowing the scanning of sinusoidal amplitude and frequency as discussed above. To minimize any interruption during the initial calibration, the gain of the RF amplifier and the bias point of MZM remain constant.

Figure 2 shows the results over four tributaries with ω = 3.77 GHz. Table 1 shows the fitting parameters and relative RMS error. The fitting curves and the measured curves almost overlap, which indicates that the proposed model in Equation (6) is very accurate. In addition, the power imbalance between tributaries and the bias point are determined accordingly.

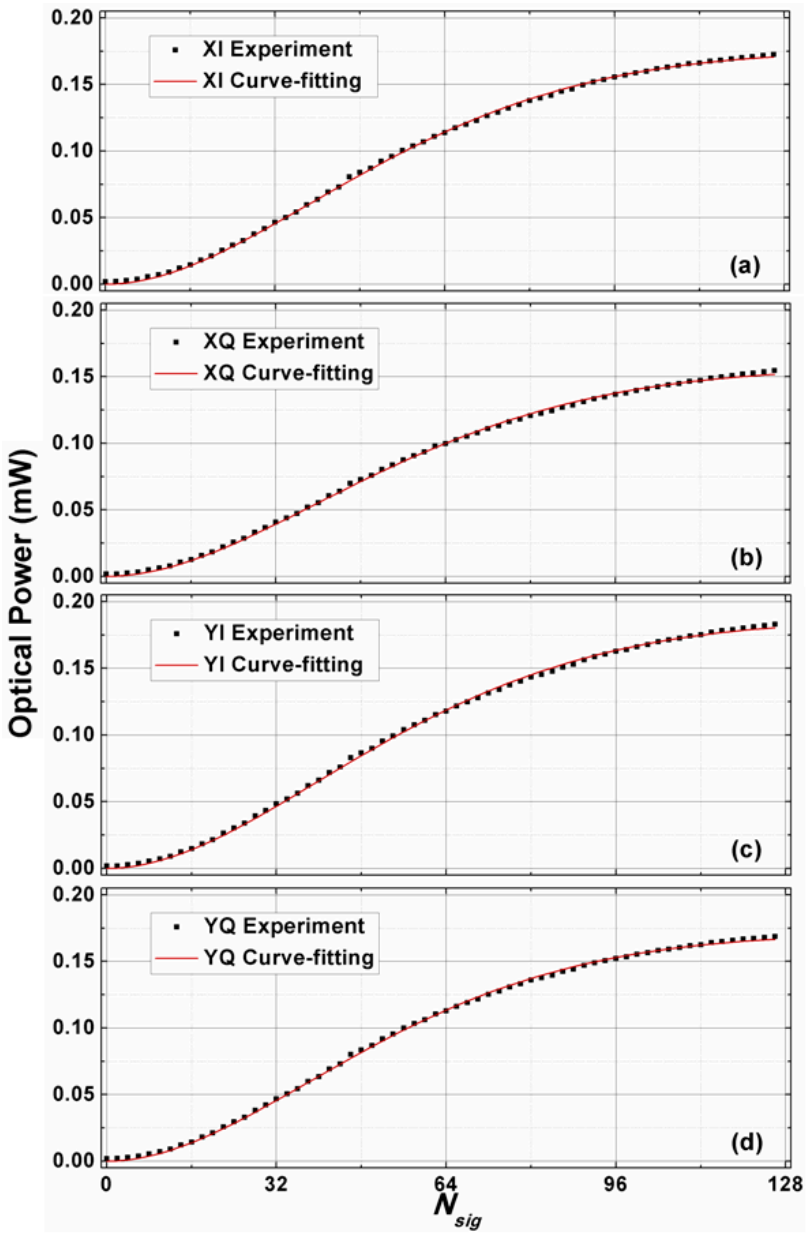

Figure 2. Measurement results versus theoretical analysis for four tributaries. ω = 3.77 GHz.

Table 1. Fittings parameters for four tributaries.

Parameters [1]	XI Trib	XQ Trib	YI Trib	YQ Trib
$P_{stdy}(mW)$	0.2712	0.2423	0.2891	0.2613
α	1.7396	1.7042	1.6991	1.7803
β	1.0000	1.0000	1.0000	1.0000
γ	−0.4503	−0.4421	−0.4429	−0.4542
Err_{rms}	4.02×10^{-2}	4.18×10^{-2}	3.95×10^{-2}	3.98×10^{-2}

[1] ω = 3.77 GHz.

Next, we scan the frequency of the sinusoidal stimulus, repeat the measurement and extract the fitting parameters. The purpose is to determine those parameters' dependency on the frequency component. Ideally, we can also extract four fitting parameters from the measurement curve. However, the output power from MZM is quite low at the high frequency close to the baud rate due to the limited bandwidth. We experience a large fitting error if we use four fitting parameters. As the steady-state power remains relatively unchanged, and the bias point has a negligible drift over time, we can assume that P_{stdy} and β remain unchanged over the different frequencies. Thus, we only extract four fitting parameters from the measurement curve using a sinusoidal stimulus running at a low-frequency ω, for example at 3.77 GHz as shown in Figure 2. We then apply the same P_{stdy} and β values to all other measurement curves at different frequencies. We extracted the fitting parameters α and γ for various frequencies. This improves the fitting error, particularly when ω is close to the baud rate. Over the different frequency, the model is accurate as shown in Figure 3.

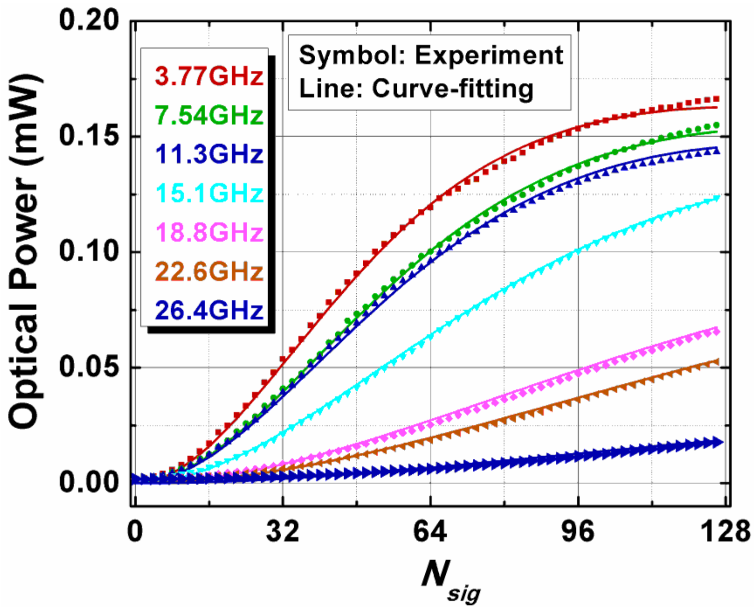

Figure 3. Results over different frequencies. Measurement results agree well with the theoretical analysis.

Then, we determine the limited bandwidth by dividing the α value at a higher frequency with the α value at 3.77 GHz, which is low enough to be used as the reference point. The limited bandwidth α is plotted in Figure 4 on the left axis. We also calculate the limited bandwidth determined through traditional power measurement. It is done through the following steps: one fixes N_{sig}, then scans ω, and measures the average output power P_{avg}. Then, the P_{avg} at the higher frequency is divided by the P_{avg} close to the DC frequency to determine the limited bandwidth. It is noticeable that both the small-signal result (for example, N_{sig} = 32) and the large-signal result (for example, N_{sig} = 127) show the deviation against the actual bandwidth (α curve). The reason is that the nonlinear response causes the actual phase shift applied to MZM to be smaller than the intended value.

The nonlinear response γ is plotted in Figure 4 towards the right axis. One can notice that within the Nyquist frequency (Ω_{NY}), the dependency of γ on ω is small. In addition, all frequency components within Ω_{NY} will have roughly the same amplitude when the limited bandwidth is compensated. Thus, we can define the average nonlinear response γ_{avg} within the Nyquist frequency. Since Nyquist pulse shaping is widely used to improve the spectral efficiency, we ignore the frequency components outside Ω_{NY} which are eliminated by the sharp roll-off of the Nyquist filter.

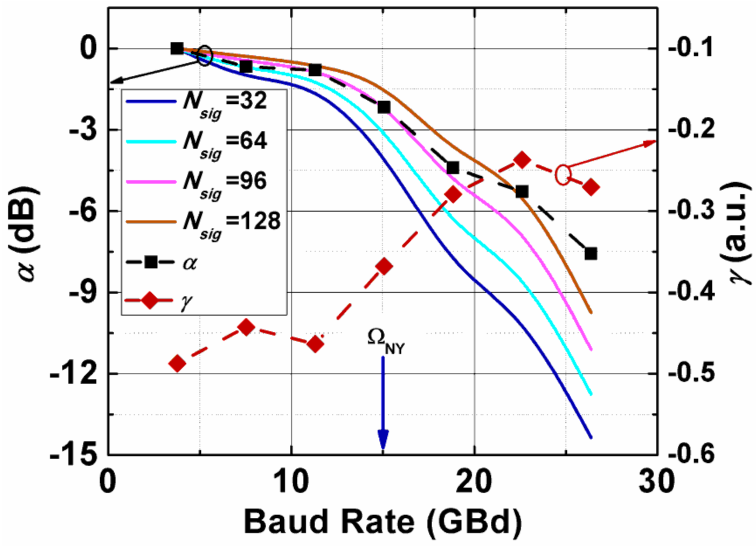

Figure 4. Bandwidth and nonlinearity of one tributary. Bandwidth is plotted on the left axis and nonlinearity is plotted on the right axis.

To mitigate the nonlinear response, a quadratic equation is first solved. There are two roots for the quadratic equation. We can choose the correct root because the normalized amplitude x is between 0 and 1. Furthermore, to obtain the coefficients of the Volterra filter for compensation of nonlinearity, a Taylor expansion is performed around the zero point, as shown below:

$$\begin{aligned} y &= \gamma_{avg}x^2 + x \\ x &= \left(\sqrt{1+4\gamma_{avg}y} - 1\right)/2\gamma_{avg} \approx y - \gamma_{avg}y^2 + 2\gamma_{avg}^2 y^3 \end{aligned}, \tag{8}$$

As seen, the coefficients of a memoryless Volterra filter are exactly the coefficients of a Taylor expansion. Thus, a third-order memoryless Volterra filter can be implemented in DSP ASIC to reverse the nonlinear response. The coefficients of the Volterra filter are simple and directly correlated to nonlinear response γ_{avg}. Furthermore, MZM's transfer function is a sinusoidal function. Its compensation function is "*arcsin*" function which can be realized through a LUT in the DSP ASIC.

As discussed in [7], the coherent transmitter can be modeled as a Wiener system, where the static nonlinear response follows the dynamic linear response. To compensate for the Wiener system, a Hammerstein system is used, where the static nonlinear equalization is placed in front of the dynamic linear equalization [19].

Figure 5 shows the block diagram of the proposed DSP architecture. The digital signal is first pre-distorted by the third-order memoryless Volterra filter to mitigate the nonlinearity. Then, the sinusoidal transfer function of the MZM is compensated by the "*arcsin*" LUT. At last, the limited bandwidth is compensated through the pre-emphasis implemented by the FIR filter. The tap coefficients of the memoryless Volterra filter is decided by γ_{avg} and the tap coefficients of the FIR filter is set such that the frequency response of the FIR filter is inversely proportional to the limited bandwidth (α).

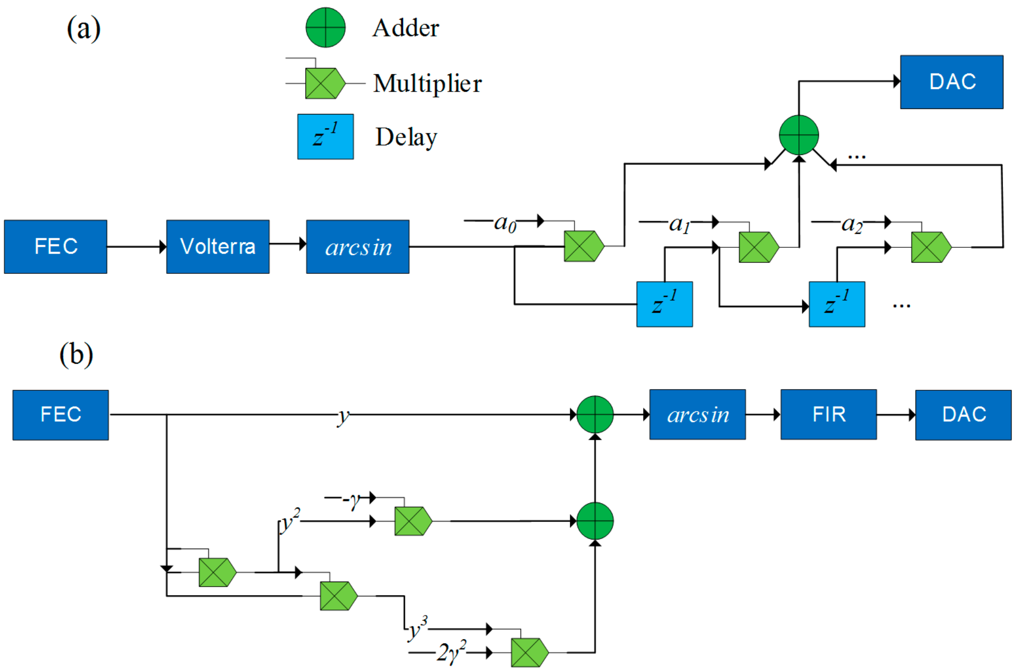

Figure 5. Proposed DSP block diagram. (**a**) The proposed structure of the FIR filter is shown in detail. a_0, a_1, a_2, and the rest are the tap coefficients determined from α. (**b**) The proposed structure of the Volterra filter is shown in detail.

3.2. Compensation for Bandwidth and Nonlinearity

To demonstrate this technique, we generate 300 Gb/s signal using 64-QAM format at approximately 30 GBd. This maximum baud rate is limited by our DSP ASIC. The DSP ASIC currently has no built-in Volterra filter. Thus, our proposed DSP architecture cannot be realized directly through the data path. So, the pseudo-random binary sequence (PRBS) is first generated. Then, the Gray coding is applied to map the QAM signal so that there is only a one-bit difference between the adjacent constellation points. Next, the memoryless Volterra filter and the '*arcsin*' function are applied to the signal. In the end, the signal is convoluted with an FIR filter. There are multiple functionalities of the FIR filter: to overcome the limited bandwidth α coming from the components on the data path; to perform Nyquist pulse shaping using root raised cosine (RRC) filter with the roll-off factor of 0.1 [20]; to compensate the skew among the tributaries [21]. The data stream is loaded into the on-chip RAM and the output of the DAC is set according to the data in the RAM.

The coherent transmitter then converts the electrical signal to an optical signal. The optical output from the coherent transmitter is further captured by a coherent receiver, which consists of 90-degree optical hybrid, balanced photodiodes, and linear trans-impedance amplifiers. An integrated tunable laser assembly (ITLA) serves as the local oscillator (LO). The electrical signal is then converted from the analog domain to the digital domain through a real-time oscilloscope (80 G samples per second, 33 GHz bandwidth).

The offline DSP is used to generate a constellation diagram and count the bit error rate. The DSP processing steps are similar to those described in [22]. First, a static equalization with a matched RRC filter is implemented in the time domain. Second, the chromatic dispersion is compensated in the frequency domain. Next, the polarization de-multiplexing and the compensation of polarization mode dispersion are implemented through an adaptive equalizer using the radius directed equalization (RDE) [23]. Then in the following steps, the timing is recovered using Gardner's method, the frequency offset is estimated, the carrier phase is recovered, and the symbol is determined. The detailed diagram for the experimental setup is shown in Figure 6.

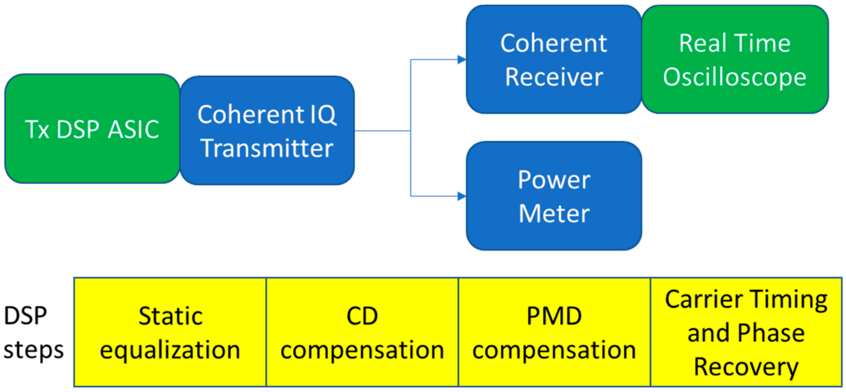

Figure 6. Experimental setup. A power meter is used to perform initial calibration with sinusoidal stimulus. Coherent receiver and real-time oscilloscope are used to recover the constellation diagram. The processing steps of DSP are also shown.

The constellation diagram can only be recovered when the limited bandwidth is compensated by the FIR filter. We compare the constellation diagram before and after the compensation of the nonlinearity, as shown in Figure 7. The gain of RF amplifier is set to a high value so that MZM is driven into a nonlinear region. As seen, without the compensation of nonlinearity, the constellation points are crowded and blurry. After the nonlinearity is mitigated, the constellation points are linearly distributed and separated.

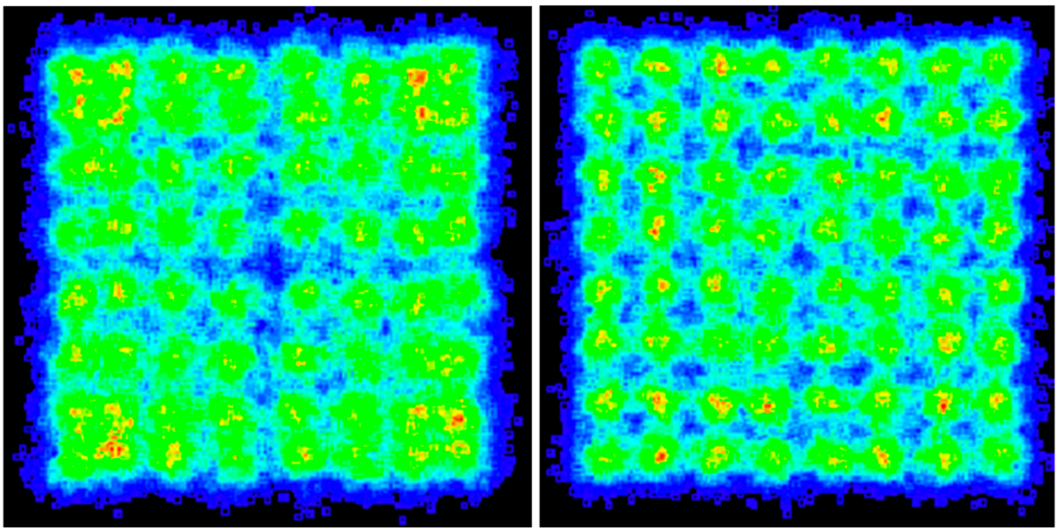

Figure 7. Constellation diagram without Volterra filter (**left**) and that with Volterra filter (**right**). Both results are obtained with bandwidth compensation and arcsin compensation.

The improvement in Q^2 factor is approximately 0.3 dB. The improvement is smaller than expected due to the hardware implementation penalty at 64-QAM. In our setup, the implementation penalty is higher than expected, mainly due to the limit effective number of bit (ENOB) in DAC and ADC. The implementation penalty acts as a noise floor for our system. The contribution from the nonlinearity is small compared with the implementation penalty. After removing the nonlinearity, the performance of the coherent transponder is still dominated by the implementation penalty. Thus, the improvement from the mitigation of the nonlinearity is smaller than expected.

4. Discussion

During the measurement of limited bandwidth and nonlinearity, we adjust the bias voltage so that the MZM is biased at its null point. The optimal bias voltage can be obtained by turning off the modulation signal and scanning the bias voltage. The bias voltage resulting in the minimum output power is the optimal voltage. The coherent IQ transmitter in our experiment is fabricated in Indium Phosphide (InP) material and its bias point is stable during the measurement. As seen from Table 1, the measured bias point factor is close to 1, indicating that the bias point is stably held at the optimal null point. During the measurement, the automatic bias control (ABC) circuit, which is based on the dithering of bias voltage, is turned off to avoid any potential interference. During the normal operation, the ABC circuit is enabled so that any long-term drift can be compensated.

In addition to the limited bandwidth (α) and the nonlinearity (γ), our method can also measure the power imbalance (P_{stdy}) among tributaries and the bias setting point (β). To achieve optimal performance, the power imbalance among the tributaries needs to be minimized. Our method offers a novel way to measure the power imbalance. Once measured, the power imbalance can be compensated by adjusting the variable optical attenuator or the semiconductor optical amplifier which can be integrated into the coherent transmitter [24]. The bias setting can be also optimized by adjusting the bias voltage applied to the MZM.

The frequency and the amplitude of the sinusoidal stimulus are controlled in the digital domain. Thus, the sinusoidal stimulus is generated with high accuracy. N_{sig} and ω can be scanned with a fine step, and the corresponding P_{avg} can be measured. It is well known that by measuring multiple data points and applying the curve fitting, the measurement accuracy can be greatly improved. Assuming K as the total measurement points, the improvement in the accuracy is proportional to the square root of K. In this way, we can significantly improve the measurement accuracy of the limited bandwidth, the nonlinearity, the power imbalance and the bias point among the four tributaries.

A Volterra filter which has multiple taps (memory) in the high-order kernels can mitigate the frequency-dependent nonlinear effect. In [7], the memory depth of the second-order kernel is 7 and the memory depth of the third order kernel is 7. Note that the frequency-dependent nonlinear response is also captured during our measurement. Thus, the coefficients of the Volterra filter with the memory can be determined accordingly. However, the Volterra filter with the memory has higher complexity, larger power consumption, and greater latency. The trade-off between performance and complexity should be carefully considered. In this work, we utilize the memoryless Volterra filter to mitigate the average nonlinearity for its simplicity. Thus, the frequency-dependent component of the nonlinearity is neglected. Still, a noticeable improvement was observed after the nonlinearity compensation was realized, particularly for MZM working in the nonlinear regime.

5. Conclusions

Next-generation coherent transponders operate at high baud rate and utilize advanced QAM modulation. For these transponders, the limited bandwidth and the nonlinearity are two severe impairments which need to be mitigated. The limited bandwidth is mitigated by the FIR filter and the nonlinearity is mitigated by the memoryless Volterra filter for its simplicity.

A novel technique to determine the tap coefficients for the FIR filter and the memoryless Volterra filter is presented. A sinusoidal stimulus is applied during the initial power-up. We then scan the amplitude and frequency of the sinusoidal stimulus and monitor the output from the coherent transmitter. Then, we use the curve fitting method to determine the underlying parameters of the coherent transmitter, such as the limited bandwidth, the nonlinearity, the power imbalance among the tributaries, and the bias point. Accordingly, we determine the tap coefficients of the FIR filter and the tap coefficients of the Volterra filter.

We apply this technique on a DSP ASIC and a coherent CFP2-ACO transponder. We drive the coherent IQ transponder into the highly nonlinear regime. When the nonlinearity is mitigated by the memoryless Volterra filter, we achieve a noticeable improvement in the constellation diagram. After the compensation of the limited bandwidth and the nonlinearity, we demonstrate a coherent IQ transponder with 300 Gb/s data rate using the 64-QAM modulation format and running at the 30 GBd baud rate.

Author Contributions: Conceptualization, methodology, software, validation, formal analysis, investigation, resources, data curation, writing—original draft preparation, writing—review and editing, visualization: Q.W. Conceptualization, methodology, software, validation, formal analysis, investigation, resources, data curation, writing—original draft preparation, writing—review and editing, visualization: Y.Y. Resources, writing—review and editing, supervision: J.A.

Funding: This research received no external funding.

Acknowledgments: The authors also gratefully acknowledge vigorous encouragement and sturdy support on innovation from Domenico Di Mola at Juniper Networks.

Conflicts of Interest: The authors declare no conflicts of interest.

References

1. Roberts, K.; Zhuge, Q.; Monga, I.; Gareau, S.; Laperle, C. Beyond 100 Gb/s: Capacity, flexibility, and network optimization. *J. Opt. Commun. Netw.* **2017**, *9*, c12–c24. [CrossRef]
2. Wang, Q.; Yue, Y.; He, X.; Vovan, A.; Anderson, A. Accurate model to predict performance of coherent optical transponder for high baud rate and advanced modulation format. *Opt. Express* **2018**, *26*, 12970–12984. [CrossRef]
3. Buchali, F.; Steiner, F.; Böcherer, G.; Schmalen, L.; Schulte, P.; Idler, W. Rate Adaptation and Reach Increase by Probabilistically Shaped 64-QAM: An Experimental Demonstration. *J. Lightwave Technol.* **2016**, *34*, 1599–1609. [CrossRef]
4. Raybon, G.; Adamiecki, A.; Cho, J.; Jorge, F.; Konczykowska, A.; Riet, M.; Duval, B.; Dupuy, J.Y.; Fontaine, N.; Winzer, P.J. 180-GBaud All-ETDM Single-Carrier Polarization Multiplexed QPSK Transmission over 4480 km. In Proceedings of the Optical Fiber Communication Conference, San Diego, CA, USA, 11–15 March 2018. paper Th4C.3.
5. Olsson, S.L.I.; Cho, J.; Chandrasekhar, S.; Chen, X.; Winzer, P.J.; Makovejs, S. Probabilistically shaped PDM 4096-QAM transmission over up to 200 km of fiber using standard intradyne detection. *Opt. Express* **2018**, *26*, 4522–4530. [CrossRef]
6. Zhang, Z.; Li, C.; Chen, J.; Ding, T.; Wang, Y.; Xiang, H.; Xiao, Z.; Li, L.; Si, M.; Cui, X. Coherent transceiver operating at 61-Gbaud/s. *Opt. Express* **2014**, *23*, 18988–18995. [CrossRef]
7. Berenguer, P.W.; Nölle, M.; Molle, L.; Raman, T.; Napoli, A.; Schubert, C.; Fischer, J.K. Nonlinear Digital Pre-distortion of Transmitter Components. *J. Lightwave Technol.* **2016**, *34*, 1739–1745. [CrossRef]
8. Khanna, G.; Spinnler, B.; Calabrò, S.; Man, E.D.; Hanik, A. A Robust Adaptive Pre-Distortion Method for Optical Communication Transmitters. *IEEE Photonics Technol. Lett.* **2016**, *28*, 752–755. [CrossRef]
9. Duthel, T.; Hermann, P.; Schiessl, J.; Fludger, C.R.S.; Bisplinghoff, C.; Kupfer, T. Characterization and Pre-Distortion of Linear and Non-Linear Transmitter Impairments for PM-64QAM Applications. In Proceedings of the European Conference and Exhibition on Optical Communications, Düsseldorf, Germany, 18–22 September 2016. paper W.4.P1.SC3.6.
10. Ke, J.; Gao, Y.; Cartledge, G.C. 400 Gbit/s single-carrier and 1 Tbit/s three-carrier super channel signals using dual polarization 16-QAM with look-up table correction and optical pulse shaping. *Opt. Express* **2014**, *22*, 71–83. [CrossRef] [PubMed]
11. Amir, I.; Bunruangses, M.; Chaiwong, K.; Udaiyakumar, R.; Maheswar, R.; Hindia, M.N.; Dimyati, K.B.; Yupapin, P. Dual-wavelength transmission system using double micro-resonator system for EMI healthcare applications. *Microsyst. Technol.* **2018**, *25*, 1185–1193. [CrossRef]
12. Amir, I.; Hindia, M.N.; Reza, A.W.; Ahmad, H. LTE smart grid performance gains with additional remote antenna units via radio over fiber using a microring resonator system. *Opt. Switch. Netw.* **2017**, *25*, 13–23. [CrossRef]
13. Hindia, M.; Qamar, F.; Rahman, T.A.; Amiri, I.S. A stochastic geometrical approach for full-duplex MIMO relaying model of high density network. *Ad Hoc Netw.* **2018**, *74*, 34–36. [CrossRef]
14. Qamar, F.; Hindia, M.N.; Abbas, T.; Dimyati, K.B.; Amiri, I.S. Investigation of QoS Performance Evaluation over 5G Network for Indoor Environment at millimeter wave Bands. *Int. J. Electron. Telecommun.* **2019**, *65*, 95–101.
15. Li, Y.; Wang, R.; Bhardwaj, A.; Ristic, S.; Bowers, J. High Linearity InP-Based Phase Modulators Using a Shallow Quantum-Well Design. *IEEE Photonics Technol. Lett.* **2010**, *22*, 1340–1342. [CrossRef]

16. Zhou, Y.; Zhou, L.; Su, F.; Li, X.; Chen, J. Linearity Measurement and Pulse Amplitude Modulation in a Silicon Single-Drive Push–Pull Mach–Zehnder Modulator. *J. Lightwave Technol.* **2016**, *34*, 3323–3329. [CrossRef]
17. Abramowitz, M.; Stegun, I. *Handbook of Mathematical Functions with Formulas, Graphs, and Mathematical Tables*; Applied Mathematics Series; Department of Commerce, National Institute of Standards and Technology: Gaithersburg, ML, USA, 1972; p. 55.
18. Lu, F.; Zhang, B.; Yue, Y.; Anderson, J.; Chang, G.-K. Investigation of Pre-Equalization Technique for Pluggable CFP2-ACO Transceivers in Beyond 100 Gb/s Transmissions. *J. Lightwave Technol.* **2017**, *35*, 230–237. [CrossRef]
19. Pan, J.; Cheng, C.-H. Wiener–Hammerstein Model Based Electrical Equalizer for Optical Communication Systems. *J. Lightwave Technol.* **2011**, *29*, 2454–2459. [CrossRef]
20. Yue, Y.; Wang, Q.; Anderson, J. Transmitter skew tolerance and spectral efficiency tradeoff in high baud-rate QAM optical communication systems. *Opt. Express* **2018**, *26*, 15045–15058. [CrossRef]
21. Yue, Y.; Zhang, B.; Wang, Q.; Lofland, R.; O'Neil, J.; Anderson, J. Detection and alignment of dual-polarization optical quadrature amplitude transmitter IQ and XY skews using reconfigurable interference. *Opt. Express* **2016**, *24*, 6719–6734. [CrossRef]
22. Faruk, M.S.; Savory, S.J. Digital Signal Processing for Coherent Transceivers Employing Multilevel Formats. *J. Lightwave Technol.* **2017**, *35*, 1125–1141. [CrossRef]
23. Fatadin, I.; Ives, D.; Savory, S.J. Blind Equalization and Carrier Phase Recovery in a 16-QAM Optical Coherent System. *J. Lightwave Technol.* **2009**, *27*, 3042–3049. [CrossRef]
24. Wang, Q.; Yue, Y.; Anderson, J. Detection and compensation of power imbalance, modulation strength, and bias drift in coherent IQ transmitter through digital filter. *Opt. Express* **2018**, *26*, 23069–23083. [CrossRef]